Charge Transport in Twisted Organic Semiconductor Crystals of Modulated Pitch

Yongfan Yang, Lygia Silva de Moraes, Christian Ruzié, Guillaume Schweicher, Yves Henri Geerts, Alan R. Kennedy, Hengyu Zhou, St. John Whittaker, Stephanie S. Lee,* Bart Kahr,* Alexander G. Shtukenberg**

Y. Yang, H. Zhou, S. J. Whittaker, Prof. S. S. Lee, Prof. B. Kahr, Prof. A. G. Shtukenberg
Department of Chemistry and Molecular Design Institute, New York University, New York, NY 10003, United States
*E-mail: stephlee@nyu.edu (Prof. S. S. Lee)
*E-mail: bart.kahr@nyu.edu (Prof. B. Kahr)
*E-mail: as5243@nyu.edu (Prof. A. G. Shtukenberg)

L. S. der Moraes, C. Ruzié, G. Schweicher, Y. H. Geerts
Laboratoire de Chimie des Polymères, Faculté des Sciences, Université Libre de Bruxelles (ULB), Boulevard du Triomphe, CP 206/01, 1050 Brussel, Belgium
*E-mail: Yves.Geerts@ulb.be (Prof. Y. H. Geerts)

Y. H. Geerts
International Solvay Institutes of Physics and Chemistry, Université Libre de Bruxelles (ULB), Boulevard du Triomphe, CP 231, 1050 Brussels, Belgium

A. R. Kennedy
University of Strathclyde, Department of Pure and Applied Chemistry, Cathedral Street 295, G1 1XL Glasgow, UK

Keywords: organic semiconductor, twisting morphology, charge transport, crystallite organization

Abstract. Many molecular crystals (approximately one third) grow as twisted helicoidal ribbons from the melt, and this preponderance is even higher in restricted classes of materials, for instance charge transfer complexes. Previously, twisted crystallites of such complexes present an increase in carrier mobilities. Here, the effect of twisting on charge mobility is better analyzed for a mono-component organic semiconductor

2,5-bis(3-dodecyl-2-thienyl)-thiazolo[5,4-d]thiazole (BDT) that forms twisted crystals with varied helicoidal pitches and makes a possible correlation with carrier mobility. These films were analyzed by X-ray scattering and Mueller matrix polarimetry to characterize the microscale organization of the polycrystalline ensembles. Carrier mobilities of organic field effect transistors were five times higher when the crystals were grown with the smallest pitches (most twisted) compared to those with the largest pitches along the fiber elongation direction. A ten-fold increase was observed along the perpendicular direction. Simulation of electrical potential based on scanning electron micrographs and density functional theory suggests that the twisting-enhanced mobility is mainly controlled by the fiber organization in the film. A greater number of tightly packed twisted fibers separated by numerous smaller gaps permits better charge transport over the film surface compared to fewer big crystallites separated by larger gaps.

1. Introduction

Flexible organic semiconductors are widely used in organic field effect transistors (OFETs), photovoltaic devices, and organic light emitting diodes and sensors.[1,2,3,4,5] Their purposeful mechanical deformations can induce so-called electromechanical responses, the coupling of strain during shearing,[6] bending[7,8,9,10] and wrinkling,[11] for example, to charge transport. Strain affects local intermolecular geometries,[12] and can modulate phonons by suppressing dynamic disorder.[9,13] Naturally, altering intermolecular interactions and vibrational frequencies can influence electronics but teasing apart the static and dynamic influences on charge mobilities will require more collective attention as electromechanical analyses of organic semiconductors appear with increasing frequency.[13,14] A unified understanding may come into focus in tandem with the basic science of mechanically dynamic molecular crystals.[15,16,17,18]

Electromechanical effects of twisting have yet to be examined. Twist-induced shearing is a mechanical deformation that can be imposed with external forces,[19,20] but twisting also spontaneously accompanies crystallization of vast collection of molecular crystalline compounds under some conditions. Fibrous molecular crystals often grow as banded spherulites composed of twisted helicoidal crystals from the melt when the driving force is high.[21,22] Our recent study of 101 single component molecular crystals (corresponding to 155 polymorphs) identified twisted morphologies from the melt in 31 % of the cases.[23] An even higher percentage (56 %) of twisted forms was observed among binary aromatic charge transfer complexes (CTCs).[24] Here we aim to understand how growth-actuated crystal twisting affects electrical properties within the context of organic semiconductors that underlie the plastic electronic industry.[25,26,27]

Previously, we studied the effect of twisting on the carrier mobilities of three tetracyanoethylene-based CTC films.[24] Density functional theory (DFT) calculations predicted a small (several percent) mobility

difference between straight and twisted single crystals with a typical twisting pitch of 10 μm. When used in OFETs, the electron mobilities were three times larger in the active layers of twisted CTC crystals compared to straight ones. The reason for the enhancement in mobilities on the devices made from twisted crystals was still unclear. A major difference between experiments and computational simulations is that the latter were performed on twisted single crystal models, whereas films are typically polycrystalline – indeed a film of a single crystal twisted around an axis parallel to the substrate would be a geometric impossibility. Active layer morphology controls overall OFET performance,[28] and the improvement of OFET mobility upon crystal twisting may arise in the organization of individual crystallites within the films compared to straight crystals. For the aforementioned CTCs, however, chemical instabilities above the melting points and relatively low absolute values of charge mobility precluded deeper analyses of the phenomena free of additional complications.

In this work, we analyze the effect of twisting on the electron and hole mobilities of 2,5-bis(3-dodecyl-2-thienyl)-thiazolo[5,4-d]thiazole (BDT, Figure 1a). BDT is a semiconductor with a conjugated heterocyclic core and two C_{12} alkyl chains.[29] The crystalline compound is especially instructive because its pitch is reliably controlled by the growth temperature (Figure 1c). Carrier mobilities measured on OFETs comprising twisted BDT crystals were found to increase up to ten times as the twisting pitch decreased by five times. Same as CTCs, computed lattice deformation in a twisted single crystal made insignificant contributions to the mobility enhancement. On the other hand, scanning electron microscopy (SEM) images collected on the surfaces of these films with varied pitches exhibited different morphologies. Twisted fibers form films with many small gaps while straight fiber films exhibited fewer but larger gaps. Discretization of the electron micrographs as networks of resistors combined with the computed anisotropy of the conductivity of single crystals permitted the computation of the scalar field of electrical potential in two dimensions. These simulations suggest that the size and distribution of these gaps is the leading factor responsible for the increased charge transport in films composed of twisted crystals with smaller pitches.

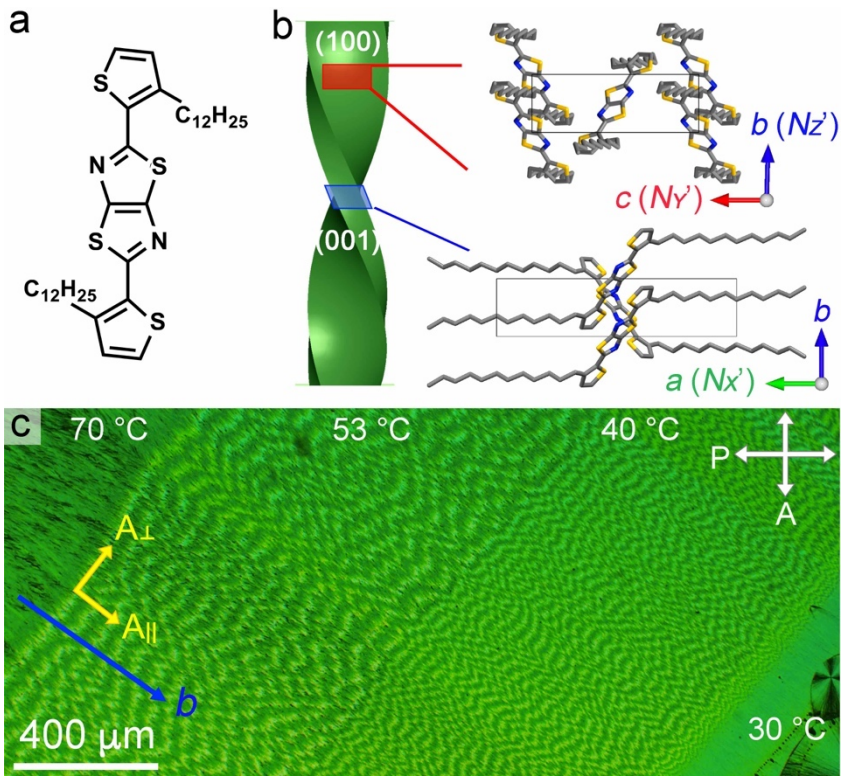

Figure 1. (a) Molecular structure of 2,5-bis(3-dodecyl-2-thienyl)-thiazolo[5,4-d]thiazole (BDT). (b) Schematic diagram of a twisted fiber and molecular packing in crystal structure. (c) BDT crystals grown at different temperatures along crystallographic *b* axis viewed under the crossed polarizer (P) and analyzer (A) as label on the right top corner.

2. Results and Discussion

2.1. Crystal Structure and Optics. BDT was prepared as previously described.[29] The structure of BDT crystals grown from solution was solved by single crystal X-ray diffraction analysis in the monoclinic space group $P2_1/c$ with a = 21.7780(2) Å, b = 5.2328(5) Å, c = 15.0645(9) Å, β = 94.135(6)° (Table S1). The conjugated thiazole rings are packed along the b axis with the distance between the mean planes of 3.47 Å, contributing to intermolecular π···π interactions (Figure 1b). Two dodecyl chains are oriented along the a axis.

Differential scanning calorimetry (DSC) was used to analyze the melting profile of BDT in two heating-cooling cycles (Figure S1). In the first heating of crystals grown from solution, an endothermic peak is observed at T_m = 73.9 °C consistent with the melting temperature of BDT. When cooling, the sample crystallization is represented by an exothermic peak at 45.1 °C. In the second heating of the sample, two endothermic peaks appear: peak 1 at 71.5 °C, and peak 2 at 73.8 °C. The second cooling cycle resulted in a similar crystallization temperature of 44.4 °C. DSC results may indicate the presence of another form of BDT once the sample crystallizes from the melt. Variable temperature powder X-ray diffraction was used to map the phase of BDT in six different temperature points from 30 °C to 72 °C, and at room temperature

(Figure S2). The experiment was conducted in two heating-cooling cycles mimicking the DSC experiment. Rietveld refinement[30,31] of powder diffraction patterns provided a good fit to a $P2_1/c$ structure solved from a single crystal XRD data (Table S2, Figure S3). In both heating cycles, unit cell parameters a, b and c do not show specific trends clustering around a = 21.72(11) Å, b = 5.19(5) Å, c = 15.08(14) Å. However, the β angle shows persistent differences between the heating of solution grown material (first run; β = 92.7(2)°), and the heating of BDT recrystallized from the melt (second run, β = 91.2(2)°). This difference may indicate small variations in the arrangement of molecules in solution and melt crystallized BDT and the second peak in DSC could signify a phase transformation between these phases. We measured the lattice constants for BDT crystallized from the melt at different temperatures. High-resolution powder X-ray diffraction data collected at Argonne National Laboratory confirmed that β angle is higher in solution grown material compared to material crystallized from the melt at 45 °C (Figure S4, Table S3). They also showed, however, that as the melt-growth temperature decreases β angle monotonically decreases across the entire temperature range and the β angle of solution-grown and melt-grown crystals at 70 °C are similar (92.16 and 92.21°, respectively). Moreover, our attempts to visualize the transformation using hot-stage microscopy were unsuccessful. This may indicate that the BDT crystal structure changes slightly as a function of crystallization conditions suggesting variations in some kind of structure disorder. The origin of the second endothermic peak in DSC is not clear but it may correspond to melting point depression of BDT fibers that have substantially smaller sizes.

BDT (1-2 mg) powder was melted at 75 °C between a glass slide and a cover slip and crystallized at various temperatures between 70 °C and room temperature, details in SI and Figure S5. With decreasing temperatures, crystallization rates first increased to a maximum of 11.5 μm/s at 60 °C. Below this temperature, growth rates decreased down to 3.5 μm/s at 30 °C. Such temperature-dependent behavior is typical for crystallization from the melt and results from a balance between increasing driving force for crystallization and decreasing molecular diffusion rates as supercooling increases[32] (Figure S7a). At crystallization temperatures above 62 °C and below 32 °C, BDT formed straight fibers (Figures 1c, S8). At intermediate crystallization temperatures, BDT crystals organized as banded spherulites with a rhythmic oscillation of transmitted light intensity. Twisting pitch, $P = \pi/\theta$, defined as the distance between successive dark or bright bands or a crystal length required to achieve a 180° rotation, decreased from over 200 μm at 62 °C to 15 μm at 35 °C (Figure S7b). This is a typical phenomenon that the twisting pitch decreases as supercooling increases because the fibers become finer.[33,34]

Several mechanisms have been proposed to explain formation of twisted crystals including (1) thermal, mechanical, compositional and electrical fields exerting stress on growing crystal; (2) strains related to dislocations; (3) unbalanced surface stress due to interactions between crystal and growth medium; (4)

heterometry stress resulting from strain between growth sectors of different composition or intergrowing crystallites in different orientations; and (5) geometrical frustrations due to mismatch between molecular arrangements corresponding to the minimum energy and translational symmetry required by a crystal lattice.[35,36] None of them, however, was unambiguously confirmed for molecular crystals growing from the melt as assemblies of fine fibers in banded spherulites. Likewise, we cannot say anything definite about origin of twisting in BDT crystals. Based on growth conditions, crystal structure and crystal morphology, we can only state that geometrical frustrations and surface stress are the most probable reasons for twisting in BDT. Typically pitch monotonically decreases as supercooling increases. As shown above, this trend is observed for BDT as well, with the exception that below 32 °C crystals become straight again. Without knowing the mechanism of twisting it is hard to say why this happens, however, one can speculate that this has something to do with slight changes of crystal structure below 32 °C (see below).

2D X-ray diffraction patterns (XRD) were collected on BDT films comprising straight and twisted fibers. Both are consistent with the diffraction pattern of a single BDT crystal grown from solution. Strong texturing was observed in the XRD pattern of straight BDT crystals, with the *h*00 family of reflections appearing along the specular direction (Figure S9a). This orientation with the {*h*00} plane parallel to the film surface is consistent with fiber growth along the <010> direction, corresponding to the intermolecular π-π stacking direction. In the XRD pattern collected on twisted BDT crystals, the diffraction peaks are broader compared than those in the XRD pattern of straight crystals and the 002 reflection is present (Figure S9b). These observations are consistent with a loss of preferred out-of-plane orientation upon crystal twisting. The 010 reflection is not observed in the XRD pattern, as expected for crystals growing in-plane along the <010> direction in our experimental configuration.

While out-of-plane orientations necessarily differ between straight and twisted crystals, the crystal structure of BDT crystals was observed to be insensitive to crystal twisting. This finding is supported by similar photoluminescence and Raman spectra collected for films with twisting pitches ranging from 20 to 120 μm (Figure S10). More detailed structure information was obtained from high-resolution powder X-ray diffraction analysis. In this method, the angular dependence of half-width maxima can provide an estimate of microstrains and mosaicity. In high-resolution powder XRD patterns collected on crystals with varying twisting pitches, diffraction peaks broadened with decreasing crystallization temperature, i.e. decreasing twisting pitch (Figure S4a).[37] Microstrains or average relative variations of interplanar distance, $\Delta d/d$, within a coherently scattering domain, approximately corresponds to the density of chaotically distributed dislocations, while mosaicity corresponds to the average size of coherently scattering domains and reflects the dislocations density in plane ensembles such as dislocation walls. Rietveld refinement of diffraction patterns using TOPAS 4.2 software demonstrated microstrains increase and mosaicity decreases as pitch

decreases (Figure S4b,c). Thus, the dislocation density (for both, chaotically distributed and organized in ensembles dislocations) increases as pitch decreases.

Straight fibers in spherulites grown at 65 °C (Figure S11) and banded spherulites with varied pitches (Figure S8) were subject to the measurement of absorption spectra in polarized light (SI). Straight fibers exhibit almost the same absorbance for light polarized parallel ($A_{\parallel}$) and normal ($A_{\perp}$) to the intermolecular π-π stacking, i.e. crystallographic *b* axis (Figure S12a). At room temperature, the polarized absorption spectrum has a maximum peak (λ_{max}) at 465 nm. For twisted fibers, dark and bright bands represent a periodic change in the orientation of crystallites from flat-on to edge-on. As shown in Figure S12b, the dichroic ratio $A_{\parallel}/A_{\perp}$ ≈ 1.7 for bright bands. Dark bands show the same spectra as straight crystals with the dichroic ratio $A_{\parallel}/A_{\perp}$ ≈ 1, independent on pitches. From the same growth direction <010> for both straight and twisted fibers, we can deduce that the dark bands of twisted crystals correspond to the flat-on orientation as straight crystals, i.e. {100} plane, and bright bands correspond to an edge-on plane (001) (Figure 1b). The absorbance was polarized along <010> consistent with π–π overlap in this direction resulting in a charge transfer band.

Mueller matrix imaging polarimetry[38,39,40,41] was used to analyze the linear retardance |LR| and circular retardance CR (see SI for *Materials and Methods*). Figure 2c,d shows the |LR| and CR micrographs (λ = 500 nm) derived from the raw Mueller matrix.[42] The birefringence calculated from |LR| oscillates between $N_{Z'} - N_{X'}$ = 0.09 for bright bands and $N_{Z'} - N_{Y'}$ = 0.04 for dark bands with $N_{Z'}$ || <010> oriented radially (Figure 2b). The radial orientation of the largest refractive index can be easily rationalized because the most polarizable group of BDT molecule, a thiazole core, makes a larger projection onto <010> direction compared to any perpendicular directions (Figure 1b). $N_{Y'} > N_{X'}$, as a consequence of the polarization of the π electrons in the aromatic cores, as opposed to polarization along the alkyl chains. CR bisects the spherulite into dextrorotatory and levorotatory halves. It oscillates smoothly from zero to a positive value in the left half (Figure 2d,e) and negative in the right half (Figure 2d,f), in phase and out of phase with |LR|, respectively. Different signs of CR indicate opposite sense of twisting for the crystallites growing along [010] and [0$\bar{1}$0] directions, consistent with the observations for $P2_1/c$ crystals twisted along the *b* axis.[43]

Straight lamellae grown at high temperature > 65 °C develop large tangential cracks, up to ~ 0.2 μm in width, to release thermoelastic stress on cooling to room temperature (Figure S9a). Straight crystals grown below 32 °C are structurally different from crystals grown at higher temperatures as evidenced by the photoluminescence and Raman spectra (Figure S10) and their charge transport properties cannot be compared directly with that of crystals grown at higher temperatures. Therefore, the following charge transport characterization was only performed for the twisted crystals with pitches varying between 30 μm and 160 μm.

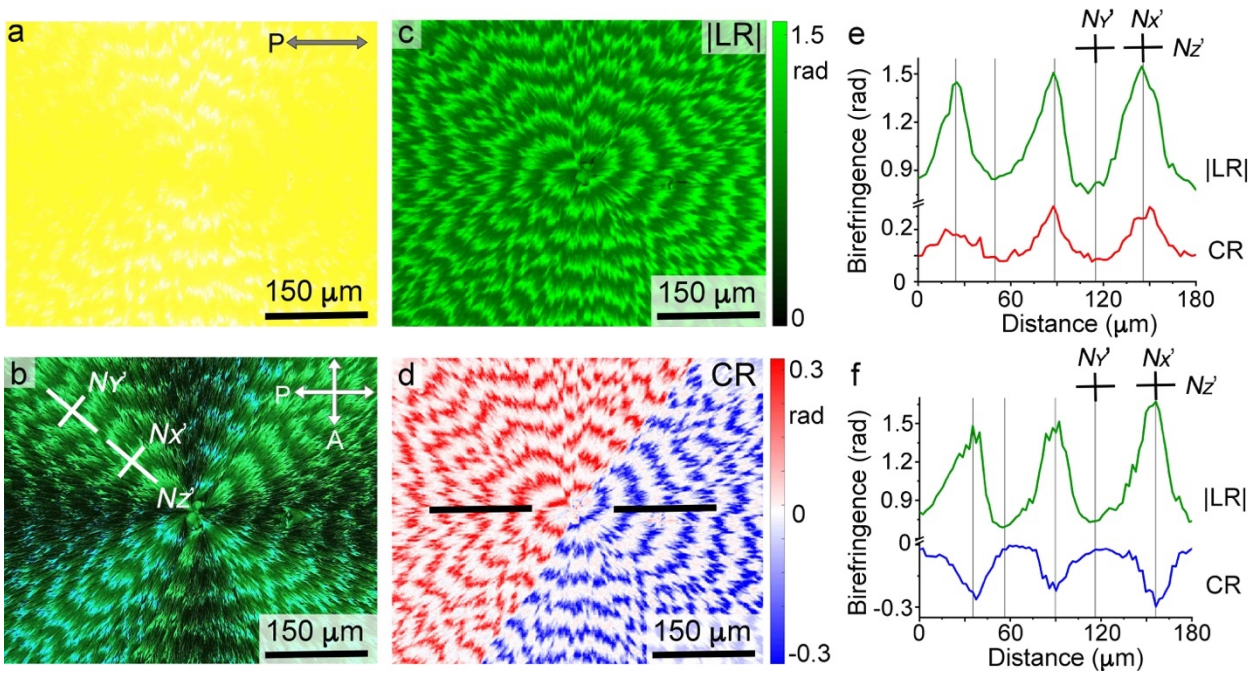

Figure 2. Twisted spherulites viewed under (a) a horizontally oriented polarizer and (b) between crossed polarizers. The directions of polarizer (P) and analyzer (A) are labeled in the right top corner. (c, d) |LR| and CR false color micrographs measured at λ = 500 nm and (e, f) extracted optical properties along the fiber growth direction depicted by black lines on the left and right side in panel (d), respectively. Growth temperature T = 50 °C.

2.2. OFET Measurements. Organic field effect transistors (OFETs) with bottom-gate bottom-contact configurations were fabricated to measure the carrier mobilities of twisted BDT films with different pitches (Figure S13). The channel length from source to drain for all devices was L = 100 µm and the width W was device-specific, typically around 2 mm.

Twisted crystals were grown on OFET device with the fiber growth direction parallel or perpendicular to the direction of current flow from the source to the drain electrodes (SI *OFET fabrication and electrical characterization*). Figure 3a displays current-voltage transfer characteristics for a representative device comprising twisted BDT crystals (P = 60 µm) and the crystal growth direction is parallel to the direction of current flow, in which the gate voltage, V_G, was swept from -80 V to 25 V at source-drain voltage, V_D = -50 V, and V_G from -30 V to 80 V at V_D = 50 V. Output characteristics of the same device are displayed in Figure S14a, b. Drain-source voltages > 50 V were not applied because the devices were easily shorted. Typically, at V_D = 50 V the output curves (Figure S14) reach the saturation regime if V_G < 60 V. At higher V_G, the saturation is not fully achieved, however, $I_D^{1/2}$ vs. V_G in the transfer curve is a straight line in the full V_G range (Figure 3) from which we extracted the charge mobility. The inability to completely achieve saturation may result in some systematic error. Minor hysteresis observed in forward and reverse scans (Figure S15) suggests slight non-ideality of the devices. These factors may change the absolute mobility

values but all data was collected in a same way, showed good reproducibility, and trended consistently. As observed from the curves, the device exhibit ambipolar transport with a hole mobility of 1×10^{-3} $cm^2V^{-1}s^{-1}$ and an electron mobility of 0.5×10^{-3} $cm^2V^{-1}s^{-1}$.

Using the same device configuration with the BDT growth direction parallel to the direction of current flow, we next measured hole and electron mobilities for BDT films of twisted crystals as a function of twisting pitch and summarized the results in Figure 3b and Table S4. Both hole and electron mobilities are higher for smaller twisting pitches. Hole mobilities increased from 0.5×10^{-3} $cm^2V^{-1}s^{-1}$ to 1.6×10^{-3} $cm^2V^{-1}s^{-1}$ for twisting pitches decreasing from P = 160 μm to P = 35 μm, respectively, and electron mobilities increased from 0.2×10^{-3} $cm^2V^{-1}s^{-1}$ to 0.8×10^{-3} $cm^2V^{-1}s^{-1}$ in the same range of twisting pitches.

We also characterized OFETs in which the crystal growth direction was perpendicular to the direction of current flow direction. Figures 3c and S14c, d display transfer and output curves, respectively, for a device with a BDT twisting pitch of 70 μm. Compared to OFETs with the growth direction parallel to the current flow direction, these devices exhibited a twenty-fold decrease in hole mobility and a 5-fold decrease in electron mobility, and electron mobility is two times higher than hole mobility. Both hole and electron mobilities increased with smaller twisting pitches, up to one order of magnitude (Figure 3d).

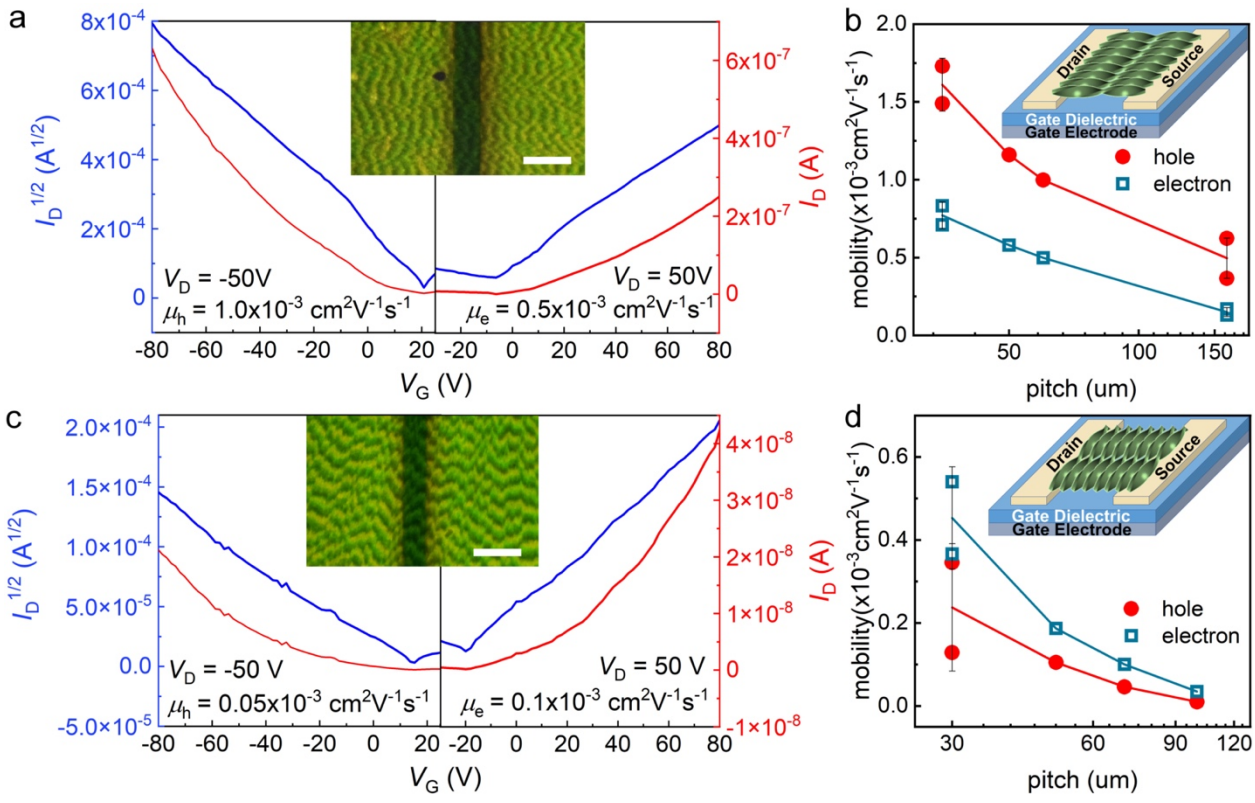

Figure 3. Representative OFET characteristics of BDT films. (a, c) Transfer curves of a representative BDT OFET with the growth direction (a) parallel and (c) perpendicular to the current flow direction. (a) Pitch P = 60 μm and channel width W = 1000 μm. (c) Pitch P = 70 μm and W = 700 μm. Channel length L = 100 μm for all devices and scale bar of the pictures in (a, c) is 200 μm. Gate dielectric capacitance per unit area C_i = 1.06×10^{-8} F/cm^2. (b, d) Hole and electron mobilities as a function of pitch for BDT OFETs with the growth direction (b) parallel and (d) perpendicular to the current flow direction. The insets of devices schematics indicate the (b) parallel and (d) perpendicular orientation of crystals fibers.

The trend of increasing mobility with decreasing pitch is inconsistent with our above finding that the defect density in these systems also increases with decreasing pitch. Because defects act as trap sites for charge carriers, OFET performance generally decreases with increasing defect density.[44,45] To understand the relationship between twisting morphology and charge mobility, we considered molecular and microstructural factors, both of which can significantly affect OFET mobilities.

2.3. Lattice misorientation in twisted single crystals. Charge mobilities through organic semiconductor films are sensitive to small atomic displacements associated with lattice deformation, as demonstrated for some bent organic semiconductor crystals.[7,10,46,47] To understand the orientation and pitch dependence of hole and electron mobilities measured in BDT OFETs, we simulated ideal orientation-dependent hole and electron mobilities in single BDT crystals according to first-principles quantum mechanics (QM) calculations and Marcus-Hush theory[48,49]. As shown in Figure 4a, thiazole rings are packed parallel to crystallographic *b* axis, and two dodecyl chains are oriented along *a*. The π-conjugated molecules provide 2D transport strongly within the stacking layer *bc*, while transport between layers, i.e. along alkyl chains, is less efficient [50] For such systems in which charge transport occurs within the molecular stacking 2D layers, the carrier mobility can be calculated from eq. (1)[51,52,53]

$$\mu_{\phi} = \frac{e}{2k_BT}\sum_i r_i^2 W_i P_i \cos^2\gamma_i \cos^2(\theta_i - \phi) \quad (1)$$

where e and k_B are the electron charge and Boltzmann constant, respectively, and the temperature T = 300 K. Index i represents a specific hopping path with a hopping distance r_i (centroid-to-centroid). γ_i is the angle between the hopping path i and *bc* plane, herein 0°. θ_i is the angle of the hopping path i projected onto *bc* layer relative to the reference *b* axis, ϕ is the orientation angle of the transistor channel to the reference *b* axis. The hopping probability P_i and hopping rate W_i are defined in the SI *Density Functional Theory Calculation* and summarized in Table S5.

Calculations of a straight BDT crystal were performed based on the crystallographic information file (SI CIF file). Figure 4c shows the DFT calculated anisotropic hole and electron mobilities of straight BDT crystals, which reflects the molecular packing motifs and relative magnitudes of electronic couplings along three hopping paths herein denotes as 12, 13 and 14 in Figure 4a. Along the intermolecular π-π stacking

direction, i.e. the crystallographic *b* axis, the hole mobility μ_h is 0.112 $cm^2V^{-1}s^{-1}$, approximately three times higher than the electron mobility μ_e. Along the *c* axis, hole mobility is 0.014 $cm^2V^{-1}s^{-1}$, one order of magnitude lower than electron mobility. Anisotropic carrier mobilities, expressed as a second rank tensor,[54,55] are summarized in Table S6. The dumbbell-shaped distribution of carrier mobility is a typical characteristic that has been reported in many other systems like rubrene[56,57] and pentacene.[58] Band structure calculations (Figure S16) gave the same anisotropic features, i.e. zero bandwidth along the crystallographic *a* axis, and a wide valence band and narrow conduction band along *b*, but narrow valence band and wide conduction band along *c*. Because of such large anisotropic transport, much research effort has focused on controlling crystal orientation during device fabrication.[59] The absolute values of the DFT-predicted mobilities are three orders of magnitude larger than the experimentally measured mobilities, as expected when comparing perfect single crystals to polycrystalline thin films with complex morphologies. The relative values of hole and electron mobilities parallel and perpendicular to the growth direction, however, are consistent between experiments and simulations.

We next performed DFT calculations of a twisted supercell to investigate the dependence of mobility on twisting pitch in BDT active layers. Mobility calculations for twisted crystals mainly involve the change of atomic coordinates related to lattice misorientation. The fiber elongation direction <010> is parallel to the hopping path 12. A supercell composed of two layers (Figure 4d) perpendicular to <010> was built to evaluate the carrier mobilities in twisted fibers. Based on the smallest experimentally observed pitch, P = 15 μm, the rotation angle between two adjacent layers around <010> was chosen as 0.01°, i.e. θ = 0.02°/nm (layers are separated by 5.2 Å). The size of the supercell, i.e. the number of unit cells in the fiber cross-section *ac*, was taken as 45 × 65 assuming that shear strain in a crystal does not exceed yield strain (γ_{max} < 0.02[60]) and thus the maximum crystal cross section size $r = 2\gamma_{max}/\theta \approx 100$ nm.[22,61] We sampled 25 evenly distributed points in the supercell and calculated average mobilities along hopping paths 12, 13, and 14. As the distance from the center increases, carrier mobilities deviate more strongly from the values for the straight crystal (Figure S17), but these changes have different signs in different directions so that the overall changes in carrier mobilities (Table S6) are not significant: hole mobility increases by 1 % along fiber elongation direction <010> and by 2 % along <001> direction; electron mobility decreases by 0.3 % along <010> and 2% along <001> direction. Thus, twisting-induced lattice misorientations cannot explain mobility differences in straight and twisted BDT crystals measured on OFETs.

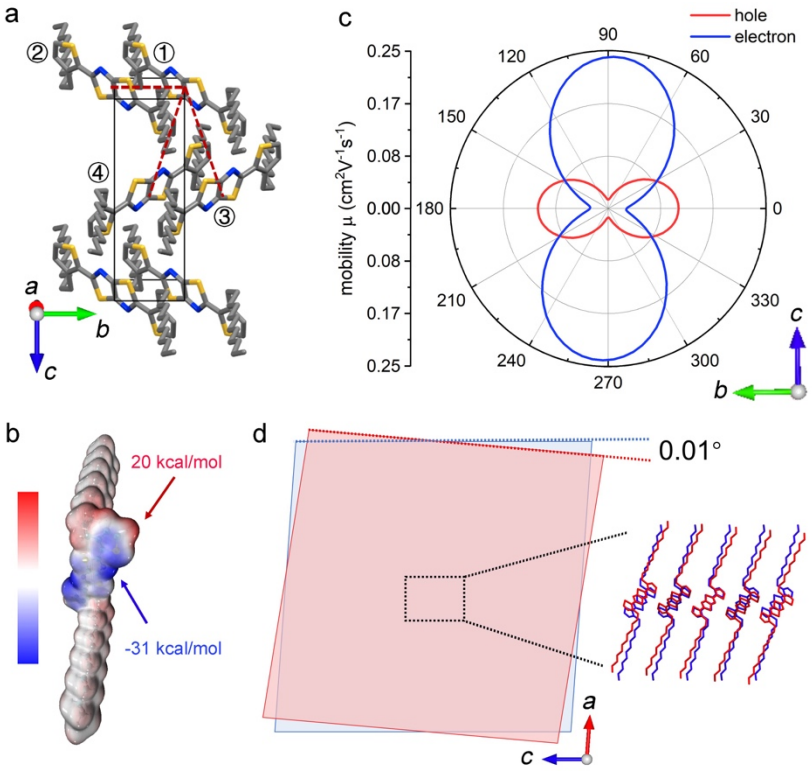

Figure 4. DFT calculation of carrier mobilities for straight and twisted BDT crystals. (a) Three hopping paths 12, 13, and 14 in crystallographic basis {*a*, *b*, *c*} viewed along *a** axis; corresponding molecules are depicted by encircled 1, 2, 3, and 4. (b) Electrostatic potential maps of a BDT molecule calculated using B3LYP/6-31G(d) in Multiwfn software.[62,63,64] (c) DFT calculated hole and electron mobilities for a straight crystal. (d) Schematic twisting model with two adjacent layers sequentially misoriented by 0.01°/5.2 Å along the *b* axis. The misorientation is exaggerated for clarity.

2.4. Microstructures in the crystallite-assembled films. Beyond molecular considerations, charge transport through the active layers of OFETs also depends strongly on the film morphology.[65,66,67] For the same compound, charge mobilities can vary by up to several orders of magnitude depending on the microstructural details of the organic semiconductor thin film.[68,69,70] To examine if differences in the microstructures of films comprising straight and twisted crystals are responsible for the observed variation in charge mobilities, we examined the surfaces of BDT films using scanning electron microscopy (SEM). Figure 5 displays optical micrographs of BDT films with varying twisting pitches, along with corresponding SEM images labeled 1 (largest pitch) to 4 (smallest pitch). The crystal surfaces are flat and comprise individual branched lamellae separated by gaps. Films with larger twisting pitches exhibit fewer but wider gaps, while films with smaller pitches exhibit more but narrower gaps. Because gaps between crystals act as barriers for charge transport, [71,72] we expect such discrepancies in the microstructure will affect charge mobilities through films with varied pitches.

To quantitatively relate film morphology and OFET performance, we turned to electrodynamic simulations. Charge transport in OFET devices occurs in a very thin (< 50 nm) surface layer of semiconductor.[73] From the cross-sectional SEM images (Figure S18), crystal films composed of straight fibers grown at 65 °C and twisted fibers with pitch of 25 μm grown at 38 °C present similar thickness, 1- 2 μm, much thicker than the charge transport layer. Therefore, the effect of different film thickness can be neglected, and the surfaces imaged by SEM can be representative of the film morphology in the charge transport region. We assume that any boundaries wider than 100 nm (all of them are visible in SEM) completely block charge transport, while in the rest of the sample mobility corresponds to its ideal value for a defect-free single crystal. Efficiency of charge transport in BDT films was further simulated by calculating conductance of the film under applied electric potential. The conductance is a product of a carrier mobility μ and carrier concentration c, which is generally not known. However, assuming that the concentration c is uniform throughout the sample, we can estimate mobility by calculating conductance.

The sample surface was considered as a rectangular grid, with all nodes connected by resistors (Figure S19). Based on Kirchhoff's and Ohm's laws, the total current flowing in and out of each node i is

$$I_i = \sum_j C_{ij}\left(U_i - U_j\right) = 0 \tag{2}$$

where C_{ij} is the conductance of the resistor connecting node i and surrounding node j, and U_i and U_j are voltages at nodes i and j, respectively. The total conductance of the network from left to right, C_{tot}, can be expressed as eq. (3), see details in SI (*Effective conductivity calculation of a resistor network)*.

$$C_{\mathrm{tot}} = \min \sum_{\text{resistor } ij} C_{ij}(U_i - U_j)^2 \tag{3}$$

Conductance values parallel and perpendicular to the fiber elongation direction were selected to account for anisotropic carrier mobilities obtained from DFT calculations. As described above, the hole mobility is higher than the electron mobility along fiber elongation direction <010>, but it is lower along the perpendicular direction <001> (Figure 4c). Figure 6 shows the calculated electric potential distribution for hole and electron transport through a film with P = 60 μm. When an electric field is applied along the fiber elongation direction, the potential is highest at the left edge and lowest at the right (Figure 6c,e). The potential drops sharply at the gaps. Therefore, the electrical potential map is consistent with the gap distribution (Figure 6a,b). In comparison, when the electric field is applied perpendicular to the fiber elongation direction, clear drops in the electric potential distribution are observed at the boundaries between fibers that run perpendicular to the electric field direction (Figure 6d,f).

The relative conductance C/C_{std} is compared for twisted films with different pitches. Here, $C_{\mathrm{std(hole)}} = \mu_{22(\mathrm{hole})}/2$ is the calculated hole conductance for an ideal film (no cracks and grain boundaries) of the

same size under the electric potential applied along the fiber elongation direction (Figure S20a), and $C_{\mathrm{std(ele)}} = \mu_{33(\mathrm{ele})}$ is the calculated electron conductance for an ideal film of the same area under the applied electric potential perpendicular to the fiber elongation direction (Figure S20d). The calculated relative conductance C/C_{std} for the film with the pitch P = 60 μm along fiber elongation direction <010> is 28% for hole transport and 68% for electron transport of the value for an ideal film, respectively. Along the perpendicular direction <001>, the relative conductance for hole and electron are 55% and 13% with respect to an ideal film, respectively.

The results of simulations for films with the pitches P = 20 μm, 35 μm, and 120 μm are shown in Figures S21-S23. Five different SEM images were taken for each pitch and the calculated relative conductance C/C_{tot} were summarized in Table S7 and Figure 6g,h. The hole conductance is higher than the electron conductance along fiber elongation direction <010> but lower along the perpendicular direction. More importantly, conductance of twisted crystals increases as the pitch decreases, showing three times larger hole conductance and 1.5 times larger electron conductance for films with the smallest pitch P = 20 μm compared with those with the largest pitch P = 120 μm along the fiber elongation direction. Perpendicular to the fiber elongation direction, hole and electron conductance are two and five times higher, respectively. Thus, a larger number of smaller gaps observed for films with smaller twisting pitches allows for better charge transport compared to a fewer number of larger boundaries observed for films with larger pitches.

The relationship between the simulated conductance and twisting pitch (Figure 3e,f) is consistent with the relationship between experimentally OFET measured mobilities and pitch (Figure 6g,h). Collectively, our results signify that the film microstructure, as determined by the twisting pitch, is the dominant factor governing twisting enhanced mobility. The pitch P is related to the crystal cross section size h, with $P \propto h^n$, n = 0.3 – 14, for h values ranging from nm to cm.[61,62] For BDT spherulites, crystallite thicknesses in films with pitches of ~ 20 μm are much smaller than those in films with pitches of ~ 120 μm (Figure S24). Smaller crystallites can occupy space more efficiently due to higher intensity of branching[74] leading to smaller-size gaps between them.[75,76] Furthermore, lamellar fibers of twisted crystals must cooperatively change orientations with neighboring fibers, potentially leading to more intimate connections between adjacent crystals compared to straight crystals that are able to grow more independently of one another.[43] The coherent, spontaneous pattern formation in banded spherulites may thus be a signature of improved contact and decreased resistance to charge transport between individual crystals.

Separating crystal size and crystal twisting contributions to the charge mobility is challenging because we cannot obtain straight and twisted crystals of precisely the same width and thickness grown at the same conditions; modulating the pitch requires changing the growth conditions. To demonstrate that both

contributions are important, we compared straight crystals grown at 32 °C with twisted crystals grown at 35 °C (Figure S8). They have similar cross sections by SEM, but their crystal structures are slightly different as evident by the Raman and fluorescence spectra (Figure S10) as well as PXRD patterns (Figure S4). For this reason, we cannot compare experimentally OFET measured mobilities directly for two films of straight crystals each grown at the temperature extremes. Polymorphism is a fascinating variable in organic electronics but it is not welcome here.[77] The calculated conductance based on the surface morphologies, however, can provide some insights. The simulated conductance of straight crystals grown at 32 °C is around 10 – 30 % lower than that of twisted crystals grown at 35 °C (Figure S25, Table S7). This conductance of straight crystal at 32 °C is substantially higher than the value obtained for the crystals with largest pitch at 120 °C, suggesting a dominant role of crystallite size. On the other hand, if twisting did not play any role, the conductance would be the same for straight crystals grown at 32 °C and twisted crystals grown at 35 °C, indicating a significant contribution of twisting to the charge transport.

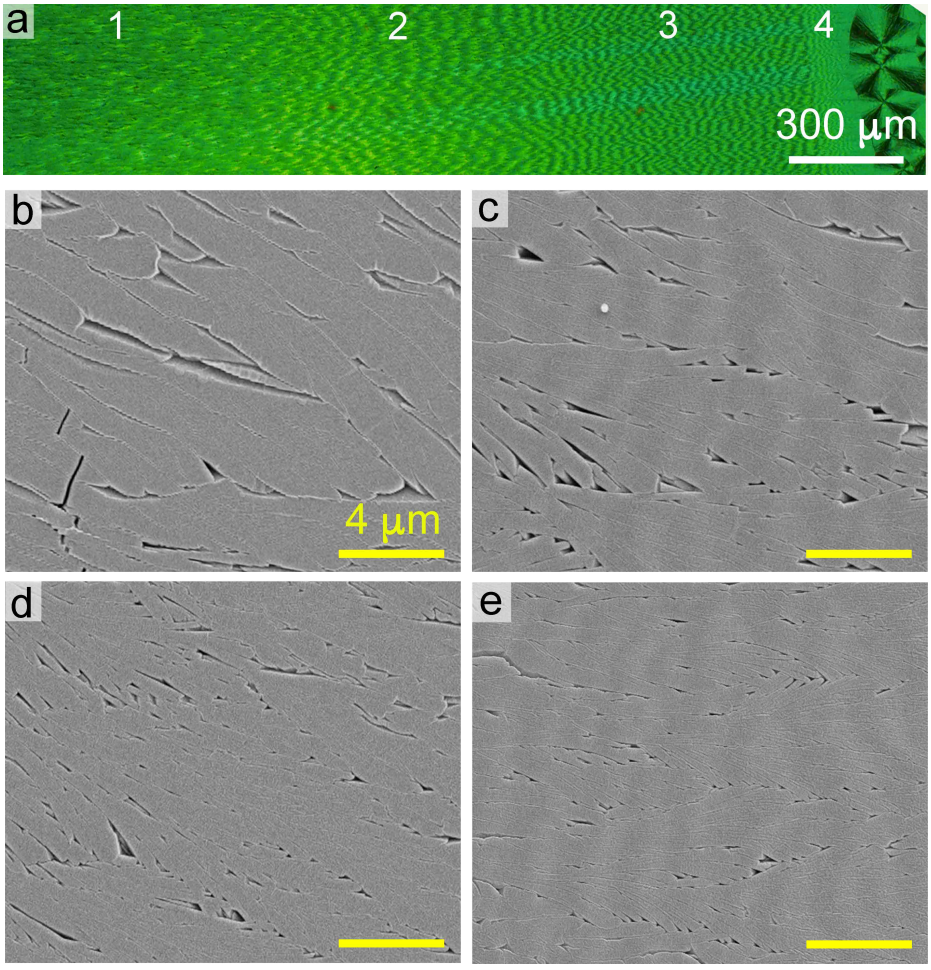

Figure 5. Optical images of BDT films comprising twisted fibers under crossed polarizers (a) and the corresponding SEM images using an Everhart-Thornley type detector with pitches of (b) 120 µm in region 1, (c) 60 µm in region 2, (d) 35 µm in region 3, and (e) 20 µm in region 4, respectively.

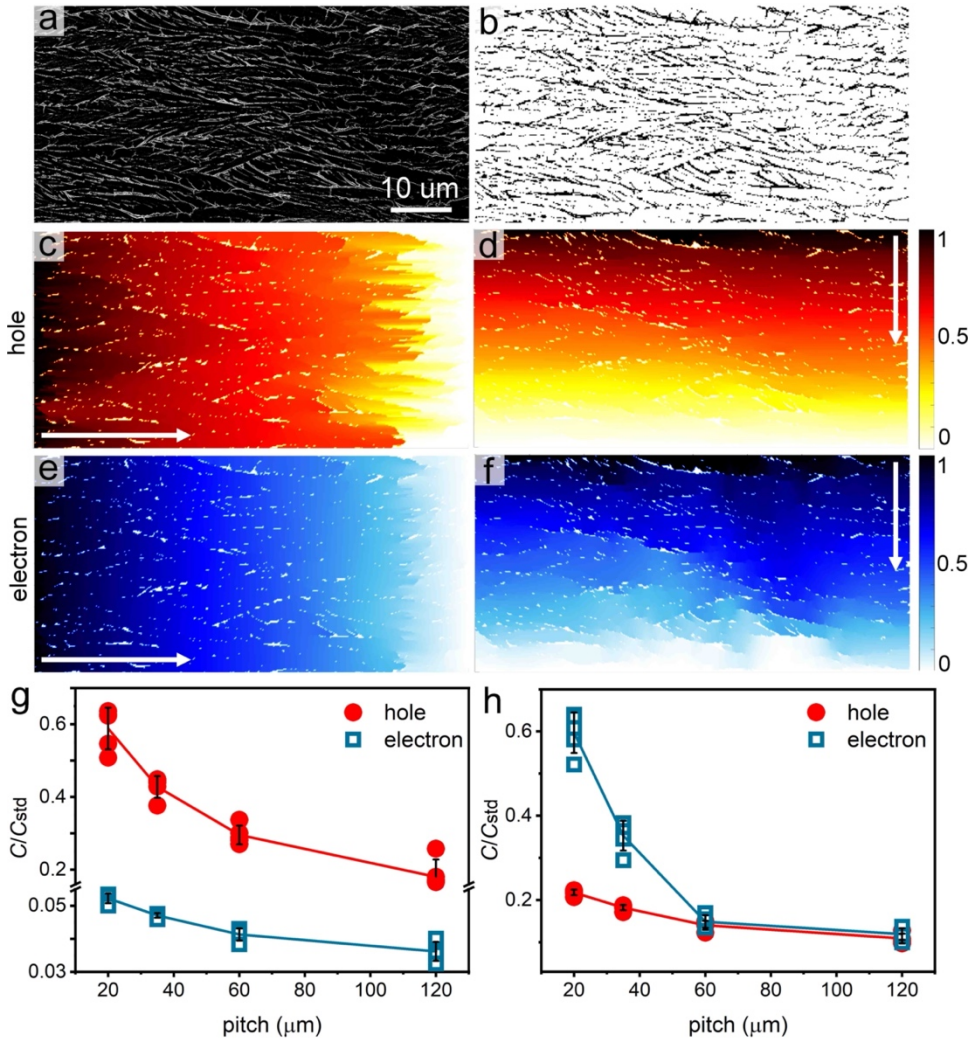

Figure 6. (a) Raw SEM image using annular secondary electron detector and (b) binary image of twisted fibers with pitch $P = 60$ μm. Calculated electric potential distribution for (c, d) hole and (e, f) electron transport under the applied electrical potential $\Delta U = 1$ V (c, e) from the left to the right side and (d, f) from the top to the bottom. Calculations for other pitches are shown in SI. (g, h) Relative conductance for hole and electron transport as a function of pitch, when the applied electric field is (g) parallel and (h) perpendicular to the fiber elongation direction. White arrows indicate the electric field direction.

3. Conclusion

From the melt, organic semiconductor BDT films consisting of spherulites with needle-like crystals growing radially outwards from nucleation centers along the intermolecular π-π stacking direction. They can twist helicoidally along the growth direction, with the twisting pitch decreasing from over 200 μm to 15 μm as growth temperature decreases. OFET measurements demonstrate four- and six-fold larger hole and electron mobilities, respectively, for twisted crystals with the smallest pitch ($P = 35$ μm), compared to the crystals with the largest pitch ($P = 160$ μm), along the crystal growth direction <010>. Along the

perpendicular direction, twisting enhanced carrier mobility is even higher by up to one order of magnitude. Using DFT simulations, we demonstrated that the twisting-enhanced mobility is not related to lattice misorientations because of the twisting deformation. SEM and electrodynamic simulations showed that fiber organization in the films, including the size and orientation of grain boundaries and cracks, is responsible for the changes in mobilities. A greater number of finer fibers with smaller gaps corresponding to twisted crystals with smaller pitches allows better charge transport along the film surface compared to a smaller number of larger crystallites separated by larger gaps in twisted crystals with larger pitches. This work highlights the importance of crystallite organization in organic semiconductor films for charge transport processes.

Supporting Information

The Supporting Information is available from the Wiley Online Library at DOI: xxx. Details of instrumental methods, OFET mobility measurements, and computational details (PDF). Accession code CCDC 2148913 contains the supplementary crystallographic data for this paper. These data can be obtained free of charge via xxx.

ORCID
Yongfan Yang: 0000-0003-3511-9733
Lygia Silva de Moraes: 0000-0001-9176-8725
Guillaume Schweicher: 0000-0002-6501-0790
Yves Geerts: 0000-0002-2660-5767
Alan R. Kennedy: 0000-0003-3652-6015
Hengyu Zhou: 0000-0001-7913-2118
St. John T Whittaker: 0000-0001-6821-8127
Stephanie S. Lee: 0000-0003-0964-6353
Bart Kahr: 0000-0002-7005-4464
Alexander G. Shtukenberg: 0000-0002-5590-4758

Acknowledgements

This work was primarily supported by the National Science Foundation DMR-2003968 and secondarily by the New York University Materials Research Science and Engineering Center (MRSEC) program of the National Science Foundation DMR-1420073. We thank Prof. Eray Aydil and Iver J. Cleveland for their help with photoluminescence measurements. We thank Prof. Robert Kohn of the Courant Institute (NYU) for his help with the conductance modeling. We thank Dr. Shenglong Wang and Song Xia for their

assistance with Gaussian and Matlab calculations on the NYU High Performance Computing (HPC) facilities. Use of the Advanced Photon Source at Argonne National Laboratory was supported by the U. S. Department of Energy, Office of Science, Office of Basic Energy Sciences, under Contract No. DE-AC02-06CH11357. Y. G. is thankful to the Belgian National Fund for Scientific Research (FNRS) for financial support through research projects: BTBT (No 2.4565.11), Phasetrans (No T.0058.14), Pi-Fast (No T.0072.18), 2D to 3D (No 30489208), and DIFFRA (No U.G001.19). Financial support from the Fédération Wallonie-Bruxelles (ARC No 20061) is also acknowledged. G. S. is a FNRS Research Associate.

Conflict of Interest

The authors declare no conflict of interest.

References

[1] H. Uoyama, K. Goushi, K. Shizu, H. Nomura, C. Adachi, *Nature* **2012**, *492*, 234.
[2] J. Mei, Y. Diao, A. L. Appleton, L. Fang, Z. Bao, *J. Am. Chem. Soc*. **2013**, *135*, 6724.
[3] V. Coropceanu, J. Cornil, D. A. da Silva Filho, Y. Olivier, R. Silbey, R.; J.-L. Bredas, *Chem. Rev*. **2007**, *107*, 926.
[4] T. M. Kelley, P. F. Baude, C. Gerlach, D. E. Ender, D. Muyres, M. A. Haase, D. E. Vogel, S. D. Theiss, *Chem. Mater*. **2004**, *16*, 4413.
[5] C. Wang, H. Dong, L. Jiang, W. Hu, *Chem. Soc. Rev*. **2018**, *47*, 422.
[6] G. Giri, E. Verploegen, S. C. B. Mannsfeld, S. Atahan-Evrenk, D. H. Kim, S. Y. Lee, H. A. Becerril, A. Aspuru-Guzik, M. F. Toney, Z. Bao, *Nature* **2011**, *480*, 504.
[7] M.-T. Ho, Y.-T. Tao, *J. Vis. Exp.* **2016**, No. e54651.
[8] S. Lai, I. Temiño, T. Cramer, F. G. der Pozo, B. Fraboni, P. Cosseddu, A. Bonfiglio, M. Mas-Torrent, *Adv. Electron Mater*. **2018**, *4*, 1700271.
[9] H. H. Choi, H. T. Yi, J. Tsurumi, J. J. Kim, A. L. Briseno, S. Watanabe, J. Takeya, K. Cho, V. Podzorov, *Adv. Sci.* **2020**, *7*, 1901824..
[10] T. Kwon, J. Y. Koo, H. C. Choi, *Angew. Chem. Int. Ed*. **2020**, *132*, 16578.
[11] M. A. Reyes-Martinez, A. J. Grosby, A. L. Briseno, *Nat. Commun.* **2015**, *6*, 1.
[12] M. K. Panda, S. Ghosh, N. Yasuda, T. Moriwaki, G. D. Mukherjee, C. M. Reddy, P. Naumov, *Nat. Chem.* **2015**, *7*, 65.
[13] T. Kubo, R. Hausermann, J. Tsurumi, J. Soeda, Y. Okada, Y. Yamashita, N. Akamatsu, A. Shishido, C. Mitsui, T. Okamoto, S. Yanagisawa, H. Matsui, J. Takeya, *Nat. Commun.* **2016**, *7*, 11156..
[14] V. Raghuwanshi, D. Bharti, A. K. Mahato, A. K. Shringi, I. Varun, S. P. Tiwari, *ACS Appl. Electron. Mater*. **2020**, *2*, 529.
[15] P. Naumov, D. P. Karothu, E. Ahmed, L. Catalano, P. Commins, J. M. Halabi, M. B. Al-Handawi, L. Li, *J. Am. Chem. Soc*. **2020**, *142*, 13256.
[16] P. Naumov, S. Chizhik, M. K. Panda, N. K. Nath, E. Boldyreva, *Chem. Rev*. **2015**, *115*, 12440.
[17] O. Sato, *Nat. Chem*. **2016**, *8*, 644.
[18] S. Saha, M. K. Mishra, C. M. Reddy, G. R. Desiraju, *Acc. Chem. Res*. **2018**, *51*, 2957.
[19] S. Saha, G. R. Desiraju, *J. Am. Chem. Soc*. **2017**, *139*, 1975.
[20] S. Saha, G. R. Desiraju, *Chem. Commun.* **2017**, *53*, 6371.
[21] F. Bernauer, *"Gedrillte" Kristalle*, Gebruder Bornträger, Berlin, **1929**.
[22] A. G. Shtukenberg, Y. O. Punin, A. Gujral, B. Kahr, *Angew. Chem. Int. Ed.* **2014**, *53*, 672.
[23] A. G. Shtukenberg, X. Zhu, Y. Yang, B. Kahr, *Cryst. Growth Des*. **2020**, *20*, 6186.
[24] Y. Yang, Y. Zhang, C. T. Hu, M. Sun, S. Jeong, S. S. Lee, A. G. Shtukenberg, B. Kahr, *Chem. Mater*. **2022**, *34*, 1778.

[25] P. Batail, *Chem. Rev*, **2004**, *104*, 4887.
[26] H. Klauk, *Organic Electronics: Materials, Manufacturing and Applications*, Wiley-VCH: Weinheim, **2006**.
[27] H. Klauk, *Organic Electronics II: More Materials and Applications*, Wiley-VCH: Weinheim, **2011**.
[28] S. S. Lee, Y.-L. Loo, *Annu. Rev. Chem. Biomol. Eng.* **2010**, *1*, 59.
[29] I. Osaka, R. Zhang, G. Sauve, D.-M. Smilgies, T. Kowalewski, R. D. McCullough, *J. Am. Chem. Soc*. **2009**, *131*, 2521.
[30] A. Albinati, B. T. M. Willis, *J. Appl. Cryst.* **1982**, *15*, 361.
[31] H. M. Rietveld, *J. Appl. Cryst.* **1969**, *2*, 65.
[32] A. G. Shtukenberg, X. Cui, J. Freudenthal, E. Gunn, E. Camp, B. Kahr, *J. Am. Chem. Soc.* **2012**, *134*, 6354.
[33] A. G. Shtukenberg, J. Freudenthal, B. Kahr, *J. Am. Chem. Soc.* **2010**, *132*, 9341.
[34] G. Ryschenkow, G. Faivre, *J. Cryst. Growth* **1988**, *87*, 221.
[35] C. Li, A. G. Shtukenberg, L. Vogt-Maranto, E. Efrati, P. Raiteri, J. D. Gale, A. L. Rohl, B. Kahr, *J. Phys. Chem. C* **2020**, *124*, 15616.
[36] A. G. Shtukenberg, R. Drori, E. V. Sturm, N. Vidavsky, A. Haddad, J. Zheng, L. A. Estroff, H. Weissman, S. G. Wolf, E. Shimoni, C. Li, N. Fellah, E. Efrati, B. Kahr, *Angew. Chem. Int. Ed.* **2020**, *132*, 14701.
[37] G. K. Williamson, W. H. Hall, *Acta Metall*. **1953**, *1*, 22.
[38] E. Fukuoka, M. Makita, Y. Nakamura, *Chem. Pharm. Bull*. **1991**, *39*, 2087.
[39] J. H. Freudenthal, E. Hollis, B. Kahr, *Chirality* **2009**, *21*, 20.
[40] X. Cui, A. G. Shtukenberg, J. Freudenthal, S. Nichols, B. Kahr, *J. Am. Chem. Soc*. **2014**, *136*, 5481.
[41] X. Cui, S. M. Nichols, O. Arteaga, J. Freudenthal, F. Paula, A. G. Shtukenberg, B. Kahr, *J. Am. Chem. Soc*. **2016**, *138*, 12211.
[42] O. Arteaga, B. Kahr, *J. Opt. Soc. Am. B*, **2019**, *36*, 72.
[43] X. Cui, A. L. Rohl, A. Shtukenberg, B. Kahr, *J. Am. Chem. Soc*. **2013**, *135*, 3395.
[44] K. Wang, M. K. Mishra, C. C. Sun, *Chem. Mater.* **2019**, *31*, 1794.
[45] M. K. Mishra, K. Mishra, S. A. S. Asif, P. Manimunda, *Chem. Commun*. **2017**, *53*, 13035.
[46] A. Landi, A. Peluso, A. Troisi, *Adv. Mater*. **2021**, *33*, 2008049.
[47] J. Elsner, S. Giannini, J. Blumberger, *J. Phys. Chem. Lett*. **2021**, *12*, 5857.
[48] R. A. Marcus, *J. Chem. Phys.* **1956**, *24*, 979.
[49] N. S. Hush, *J. Chem. Phys.* **1958**, *28*, 962.
[50] Y. Hu, D. X. Cao, A. T. Lill, L. Jiang, C.-A. Di, X. Gao, H. Sirringhaus, T.-Q. Nguyen, *Adv. Electron. Mater.* **2018**, *4*, 1800175.
[51] L. Zhu, Y. Yi, Y. Li, E.-G. Kim, V. Coropceanu, J.-L. Bredas, *J. Am. Chem. Soc.* **2012**, *134*, 2340.
[52] S.-H. Wen, A. Li, J. Song, W.-Q. Deng, K.-L. Han, W. A. Goddard III, *J. Phys. Chem. B* **2009**, *113*, 8813.
[53] Y. Zhang, Y. Duan, L. Song, D. Zheng, M. Zhang, G. Zhao, *J. Chem. Phys*. **2017**, *147*, 114905.
[54] D. R. Lovett, *Tensor properties of crystals*. 2nd ed.; Institute of Physics Pub.: Philadelphia, **1999**; p xiii, 166 p.
[55] J. F. Nye, *Physical properties of crystals : their representation by tensors and matrices*. 1st published in pbk. with corrections, 1984. ed.; Clarendon Press; Oxford University Press: Oxford Oxfordshire, New York, **1984**.
[56] V. C. Sundar, J. Zaumseil, V. Podzorov, E. Menard, R. L. Willett, T. Someya, M. E. Gershenson, J. A. Rogers, *Science* **2004**, *303*, 1644.
[57] M.-M. Ling, C. Reese, A. L. Briseno, Z. Bao, *Synth. Met.* **2007**, *157*, 257.
[58] J. Y. Lee, S. Roth, Y. W. Park, *Appl. Phys. Lett.* **2006**, *88*, 252106.
[59] W. Deng, X. Zhang, H. Dong, J. Jie, X. Xu, J. Liu, L. He, L. Xu, W. Hu, X. Zhang, *Mater. Today* **2019,** *24*, 17.
[60] A. G. Shtukenberg, A. Gujral, E. Rosseeva, X. Cui, B. Kahr, *CrystEngComm* **2015**, *17*, 8817.
[61] H. J. Frost, M. F. Ashby, *Deformation-mechanism maps : the plasticity and creep of metals and ceramics*. 1st ed.; Pergamon Press: Oxford Oxfordshire ; New York, **1982**; p ix, 166 p.
[62] A. Becke, *J. Chem. Phys.* **1993**, *98*, 5648.
[63] W. J. Hehre, R. Ditchfield, J. A. Pople, *J. Chem. Phys.* **1972**, *56*, 2257..
[64] T. Lu, F. Chen, *J. Comput. Chem.* **2012**, *33*, 580.
[65] J. Locklin, M. E. Roberts, S. C. B. Mannsfeld, Z. Bao, *J. Macromol. Sci. Polym. Rev.* **2006**, *46*, 79.
[66] F. Liu, C. Wang, J. K. Baral, L. Zhang, J. J. Watkins, A. L. Briseno, T. P. Russell, *J. Am. Chem. Soc.* **2013**, *135*, 19248.
[67] Y. Huang, J. Sun, J. Zhang, S. Wang, H. Huang, J. Zhang, D. Yan, Y. Gao, J. Yang, *Org. Electron.* **2016**, *36*, 73.
[68] S. S. Lee, C. S. Kim, E. D. Gomez, B. Purushothaman, M. F. Toney, C. Wang, A. Hexemer, J. E. Anthony, Y.-L. Loo, *Adv. Mater.* **2009**, *21*, 3605.

[69] A. F. Paterson, S. Singh, K. J. Fallon, T. Hodsden, Y. Han, B. C. Schroeder, H. Bronstein, M. Heeney, I. McCulloch, T. D. Anthopoulos, *Adv. Mater.* **2018**, *30*, 1801079.
[70] Y. Diao, L. Shaw, Z. Bao, S. C. Mannsfeld, *Energy Environ Sci.* **2014**, *7*, 2145.
[71] T. H. Ly, D. J. Perello, J. Zhao, Q. Deng, H. Kim, G. H. Han, S. H. Chae, H. Y. Jeong, Y. H. Lee, *Nat. Commun.* **2016**, *7*, 10426.
[72] F. Giannazzo, M. Bosi, F. Fabbri, E. Schilirò, G. Greco, F. Roccaforte, *Phys. Status Solidi RRL* **2020**, *14*, 1900393..
[73] A. Dodabalapur, L. Torsi, H. E. Katz, *Science* **1995**, *268*, 270.
[74] A. G. Shtukenberg, Y. O. Punin, E. Gunn, B. Kahr, *Chem. Rev.* **2012**, *112*, 1805.
[75] S. Sasaki, Y. Sakaki, A. Takahara, T. Kajiyama, *Polymer* **2002**, *43*, 3441.
[76] M. Hütter, P. J. in't Veld, G. C. Rutledge, *Polymer* **2006**, *47*, 5494.
[77] H. Chung, Y. Diao, *J. Mat. Chem. C*, **2016**, *4*, 3915.